


Full-wave Tailoring Between Different Elastic Media: A Double-Unit Elastic Metasurface

Sung Won Lee ¹, Ye Jeong Shin,¹ Hong Woo Park ¹, Hong Min Seung,^{2,3,*} and Joo Hwan Oh ^{1,†}

¹*School of Mechanical Engineering, Ulsan National Institute of Science and Technology, UNIST-gil 50, Eonyang-eup, Ulju-gun, Ulsan 44919, South Korea*

²*AI Metamaterial Research Team, Korea Research Institute of Standards and Science, Gajeong-ro 267, Yuseong-gu, Daejeon, 34113, South Korea*

³*Department of Science of Measurement, University of Science and Technology (UST), Gajeong-ro 207, Yuseong-gu, Daejeon 34113, South Korea*

 (Received 6 October 2021; revised 16 November 2021; accepted 18 November 2021; published 6 December 2021)

We present a study of full-wave tailoring with an elastic metasurface between two different media. Unlike previous research on elastic metasurface, the current study has a crucial difference that the metasurface is placed between two different media. Interestingly, we find that previous studies have a theoretical limitation that negates the simultaneous achievement of various phase shifts and full transmission between inhomogeneous media. To overcome this, we propose a double-unit elastic metasurface composed of two units, phase modulator and impedance matcher, to avoid the constraint restricting various phase shifts with full transmission. Numerical and experimental investigations are performed to validate the operation of the double-unit elastic metasurface. The proposed metasurface is expected to be applied in various ultrasonic applications.

DOI: [10.1103/PhysRevApplied.16.064013](https://doi.org/10.1103/PhysRevApplied.16.064013)

I. INTRODUCTION

Metasurfaces are artificial subwavelength layers that tailor wave fronts to achieve a simple manipulation of wave directions [1–14], holography [15–17], or cloaking [18–21]. As a frontier research area in electromagnetics [1–9], metasurfaces have been actively studied in acoustics [10,11,16,17,20,21] and elastics [12–14,22–26]. In general, metasurfaces can be categorized into two types: reflection- [6–11] and refraction-type metasurfaces [1–5]. Reflection-type metasurfaces are designed for reflected wave tailoring and commonly attached at the edge of the medium. Conversely, refraction-type metasurfaces are designed for transmitted wave tailoring and commonly located inside a homogeneous medium. Refraction-type metasurfaces have received considerable attention because the relevant physics and related applications cover a much broader spectrum than that of reflection-type metasurfaces. To specify, whereas the reflection-type needs only the common condition to fulfill various phase shifts from 0 to 2π rad, the refraction types require additional full-transmission condition.

Despite the active studies conducted on refraction-type elastic metasurfaces [12–14], previous research on refraction-type elastic metasurfaces have focused on the homogeneous case where wave media before and after metasurface are the same. Here, we consider the inhomogeneous case—what will happen if the wave media before and after metasurface are different? Here, we find that the previous methods used for homogeneous case cannot be applied for wave-front tailoring in the inhomogeneous case. To be specific, we find that with the previous methods, the two conditions of refraction type, various phase shifts from 0 to 2π rad and full transmission, cannot be satisfied simultaneously. If the full-transmission condition is satisfied, only the fixed phase shift of 90° and 270° can be achieved; hence, the condition of variable phase shift cannot be satisfied. Thus, in the inhomogeneous case, the previous methods can only provide limited wave-front tailoring—the wave-front tailoring with significant reflection or full transmission without wave-front tailoring [27,28], as shown in Figs. 1(a) and 1(b). Particularly, this issue becomes more critical in elastics where various wave media are involved in almost all applications [29,30], unlike in acoustics or electromagnetics where almost all applications are the homogeneous case in air or water, etc. Nevertheless, there have been no research on the elastic metasurface realizing wave-front tailoring in inhomogeneous cases.

*Co-corresponding Author. shm@kriss.re.kr

†Corresponding Author. joohtwan.oh@unist.ac.kr

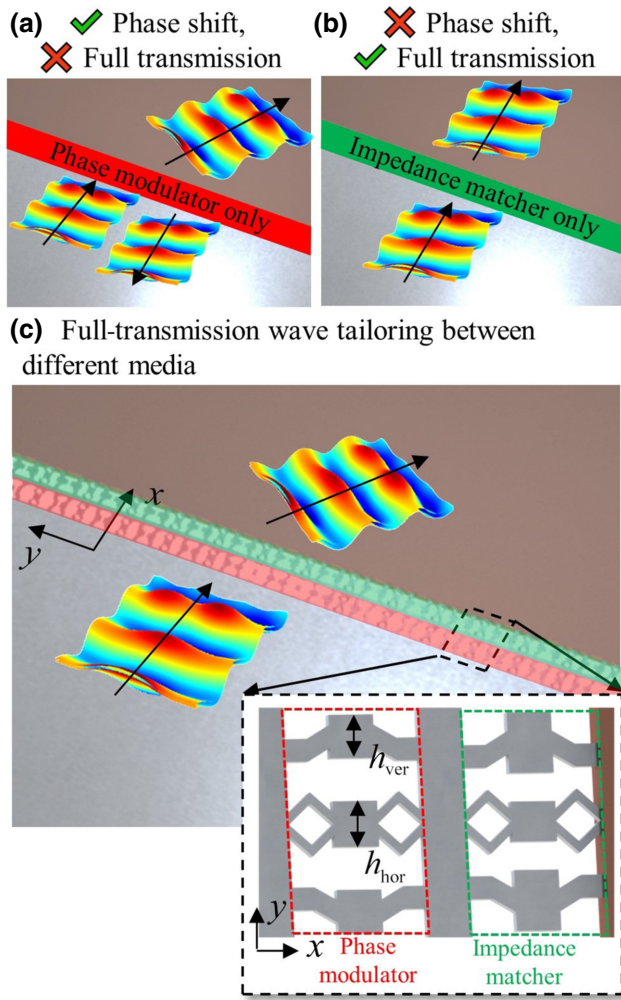


FIG. 1. Schematics of various anomalous refractions by (a) phase modulator only, (b) impedance matcher only, and (c) double-unit metasurface consisting of both phase modulator and impedance matcher.

In addition, we propose a solution that achieves full-wave control between the elastic inhomogeneous media case. The key idea is a double-unit metasurface consisting of two different units, the phase modulator and the impedance matcher as can be seen in Fig. 1(c). Here, the phase modulator is installed inside the incident medium so that the wave medium before and after the unit is the same. If the wave is incident to the metasurface, the phase modulator provides proper phase shift. Subsequently, the transmitted waves encounter the impedance matcher where the wave medium changes. Because it is impossible to achieve both phase shift and full transmission, the impedance matcher provides only full transmission between two different media. As a result, wave-front tailoring with full transmission is feasible with the double-unit metasurface. Numerical simulations and experiments are conducted to support our proposal.

II. BACKGROUND THEORY: THE CONSTANT PHASE-SHIFT LIMITATION UNDER FULL TRANSMISSION OF THE PREVIOUS METHODS

First, we briefly show why full-transmission wavefront tailoring between inhomogeneous media cannot be achieved with the previous refraction-type metasurface methods. Previously, the refraction-type full-transmission elastic metasurface has been modeled as a thin layer realizing material property [13] or a single mass-spring system [14,26]. Here, we install these methods between inhomogeneous media as in Figs. 2(a) and 2(b), respectively, to examine phase shift with full transmission. The variable A is the amplitudes of the forward-propagating waves, while B is for the backward-propagating waves. Also, the subscripts 1 and 2 are used for the waves at the left media and right media, respectively.

For the first method shown in Fig. 2(a), it is well known that the transmission $T = A_2/A_1$ through the metasurface layer can be calculated as

$$T = \frac{4Z_1Z_m}{e^{-ik_mL}(Z_2 - Z_m)(Z_m - Z_1) + e^{ik_mL}(Z_2 + Z_m)(Z_m + Z_1)}, \quad (1)$$

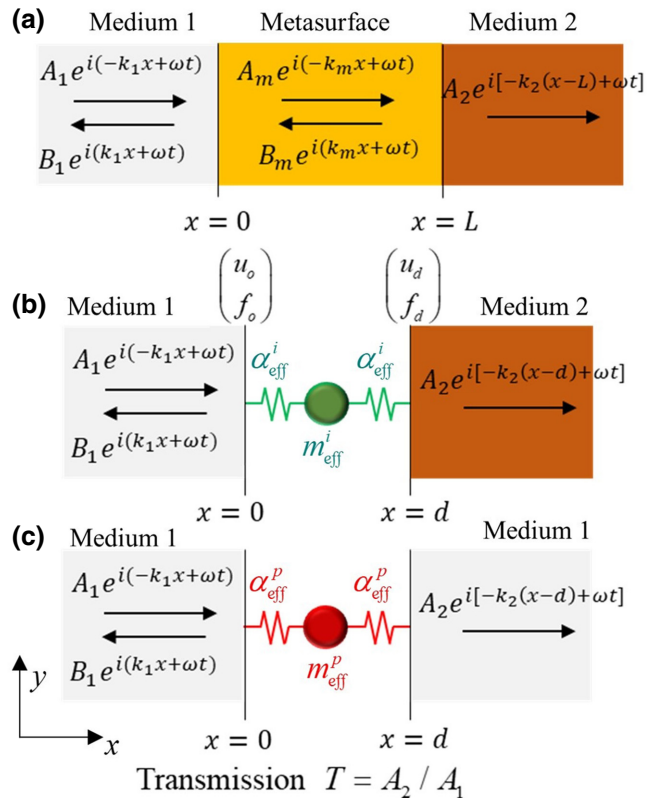


FIG. 2. Schematics of (a) the previous layer metasurface method and single mass-spring metasurface units for (b) impedance matcher and (c) phase modulator.

where Z_1 , Z_2 , and Z_m are the characteristic impedance of medium 1, medium 2, and the metasurface, respectively. It is well known that the full-transmission conditions are $L = (2n - 1)\lambda/4$ ($n = 1, 2, \dots$) and $Z_m = \sqrt{Z_1 Z_2}$ [29]. With these conditions, the transmission is defined as a purely imaginary value of $T = i\sqrt{Z_1/Z_2}$. This indicates that the phase shift should be 90° under the full-transmission conditions. In other words, using the previous layer method, if the full transmission is achieved, various phase shifts from 0 to 2π rad cannot be achieved.

In Fig. 2(b), which is the schematic figure of the second previous method, u_o, u_d refer to the displacements and f_o, f_d refer to the traction forces at the left and right boundaries, respectively. The dynamic equation of the mass-spring unit can be derived as

$$m_{\text{eff}}^i \frac{\partial^2 u}{\partial t^2} = \alpha_{\text{eff}}^i (u_o + u_d - 2u), \quad (2)$$

$$f_o = \alpha_{\text{eff}}^i (u - u_o), \quad (3)$$

$$f_d = \alpha_{\text{eff}}^i (u_d - u). \quad (4)$$

Assuming simple harmonic motion with an angular frequency ω , Eqs. (2)–(4) can be rearranged into a linear equation with effective parameters as

$$u = \frac{\alpha_{\text{eff}}^i}{2\alpha_{\text{eff}}^i - \omega^2 m_{\text{eff}}^i} (u_o + u_d), \quad (5)$$

$$u_d = \frac{\alpha_{\text{eff}}^i - \omega^2 m_{\text{eff}}^i}{\alpha_{\text{eff}}^i} u_o + \frac{2\alpha_{\text{eff}}^i - \omega^2 m_{\text{eff}}^i}{\alpha_{\text{eff}}^i} f_o, \quad (6)$$

$$f_d = -\omega^2 m_{\text{eff}}^i u_o + \frac{\alpha_{\text{eff}}^i - \omega^2 m_{\text{eff}}^i}{\alpha_{\text{eff}}^i} f_o. \quad (7)$$

Therefore, the relationship between the displacements and traction forces can be described in the matrix form, which is well known as the transfer matrix [13,14,26], as

$$\begin{pmatrix} u_d \\ f_d \end{pmatrix} = \mathbf{T} \begin{pmatrix} u_o \\ f_o \end{pmatrix}, \quad (8)$$

where

$$\mathbf{T} = \begin{pmatrix} T_{11} & T_{12} \\ T_{21} & T_{22} \end{pmatrix} = \begin{pmatrix} \frac{\alpha_{\text{eff}}^i - \omega^2 m_{\text{eff}}^i}{\alpha_{\text{eff}}^i} & \frac{2\alpha_{\text{eff}}^i - \omega^2 m_{\text{eff}}^i}{\alpha_{\text{eff}}^i} \\ -\omega^2 m_{\text{eff}}^i & \frac{\alpha_{\text{eff}}^i - \omega^2 m_{\text{eff}}^i}{\alpha_{\text{eff}}^i} \end{pmatrix}. \quad (9)$$

By using the transfer matrix, the wave transmission can be derived. The harmonic displacements at the left and right

media can be derived as at $x \leq 0$ (at the left medium):

$$u_i = (A_1 e^{-ik_1 x} + B_1 e^{ik_1 x}) e^{i\omega t}, \quad (10)$$

at $x \geq d$ (at the right medium):

$$u_t = A_2 e^{-ik_2(x-d)} e^{i\omega t}, \quad (11)$$

where A_1, B_1 , and A_2 are the amplitudes seen in Fig. 2(b). Here, the force can be calculated easily by using the mechanical impedance $Z = \rho c A$ as $f = C_{11} (\partial u / \partial x)$ (C_{11} refers the x -directional component of the stiffness tensor in Voigt notation). Using these relations, the displacements and forces at the left and right media can be derived as the functions of the wave amplitudes as at $x \leq 0$ (at the left medium):

$$\begin{pmatrix} u_i \\ f_i \end{pmatrix} = \begin{pmatrix} e^{-ik_1 x} & e^{ik_1 x} \\ -i\omega Z_1 e^{-ik_1 x} & i\omega Z_1 e^{ik_1 x} \end{pmatrix} \begin{pmatrix} A_1 \\ B_1 \end{pmatrix} e^{i\omega t}, \quad (12)$$

at $x \geq d$ (at the right medium):

$$\begin{pmatrix} u_t \\ f_t \end{pmatrix} = \begin{pmatrix} e^{-ik_2(x-d)} & e^{ik_2(x-d)} \\ -i\omega Z_2 e^{-ik_2(x-d)} & i\omega Z_2 e^{ik_2(x-d)} \end{pmatrix} \begin{pmatrix} A_2 \\ 0 \end{pmatrix} e^{i\omega t}. \quad (13)$$

Here, one can obtain the boundary conditions by inputting $x = 0$ and $x = d$ into Eqs. (12) and (13), respectively, as

$$\begin{pmatrix} u_o \\ f_o \end{pmatrix} = \mathbf{M}_1 \begin{pmatrix} A_1 \\ B_1 \end{pmatrix} e^{i\omega t}, \quad (14)$$

$$\begin{pmatrix} u_d \\ f_d \end{pmatrix} = \mathbf{M}_2 \begin{pmatrix} A_2 \\ 0 \end{pmatrix} e^{i\omega t}, \quad (15)$$

where

$$M_i = \begin{pmatrix} 1 & 1 \\ -i\omega Z_i & i\omega Z_i \end{pmatrix}. \quad (16)$$

Substituting Eqs. (14) and (15) into Eq. (8), one can derive the matrix equation between left and right media amplitudes as

$$\begin{pmatrix} A_2 \\ 0 \end{pmatrix} = \mathbf{M}_2^{-1} \mathbf{T} \mathbf{M}_1 \begin{pmatrix} A_1 \\ B_1 \end{pmatrix} = \mathbf{S} \begin{pmatrix} A_1 \\ B_1 \end{pmatrix}, \quad (17)$$

where

$$S_{11} = \frac{i\omega Z_2 T_{11} - T_{21} - i^2 \omega^2 Z_1 Z_2 T_{12} + i\omega Z_1 T_{22}}{2i\omega Z_2}, \quad (18a)$$

$$S_{12} = \frac{i\omega Z_2 T_{11} - T_{21} + i^2 \omega^2 Z_1 Z_2 T_{12} - i\omega Z_1 T_{22}}{2i\omega Z_2}, \quad (18b)$$

$$S_{21} = \frac{i\omega Z_2 T_{11} + T_{21} - i^2 \omega^2 Z_1 Z_2 T_{12} - i\omega Z_1 T_{22}}{2i\omega Z_2}, \quad (18c)$$

$$S_{22} = \frac{i\omega Z_2 T_{11} + T_{21} + i^2 \omega^2 Z_1 Z_2 T_{12} + i\omega Z_1 T_{22}}{2i\omega Z_2}. \quad (18d)$$

Since determinants of the matrix \mathbf{T} , \mathbf{M}_1 , \mathbf{M}_2 are not zero, Eq. (17) can be inverted as

$$\begin{pmatrix} A_1 \\ B_1 \end{pmatrix} = \frac{1}{\det(\mathbf{S})} \begin{pmatrix} S_{22} & -S_{12} \\ -S_{21} & S_{11} \end{pmatrix} \begin{pmatrix} A_2 \\ 0 \end{pmatrix}. \quad (19)$$

Therefore, the transmission coefficient can be easily derived as

$$\begin{aligned} T &= \frac{A_2}{A_1} = \frac{\det(\mathbf{S})}{S_{22}} \\ &= \frac{2i\omega Z_1}{i\omega Z_2 T_{11} + T_{21} + i^2 \omega^2 Z_1 Z_2 T_{12} + i\omega Z_1 T_{22}}. \end{aligned} \quad (20)$$

Also, the reflection coefficient can be calculated as

$$-\frac{S_{21}}{\det(\mathbf{S})} A_2 = B_1, \quad R = \frac{B_1}{A_1} = -\frac{S_{21}}{S_{22}}. \quad (21)$$

Here, we focus on the reflection coefficient because at the full transmission the reflected energy should be zero. The reflection coefficient can be rearranged as

$$\begin{aligned} -\frac{S_{21}}{S_{22}} &= -\frac{i\omega Z_2 T_{11} + T_{21} - i^2 \omega^2 Z_1 Z_2 T_{12} - i\omega Z_1 T_{22}}{i\omega Z_2 T_{11} + T_{21} + i^2 \omega^2 Z_1 Z_2 T_{12} + i\omega Z_1 T_{22}} \\ &= -\frac{T_{21} + \omega^2 Z_1 Z_2 T_{12} + i\omega(Z_2 - Z_1)T_{11}}{T_{21} - \omega^2 Z_1 Z_2 T_{12} + i\omega(Z_2 + Z_1)T_{11}}. \end{aligned} \quad (22)$$

Note that in this mass-spring unit, the transfer-matrix elements T_{11} and T_{22} are identical. Therefore, the norm of the reflection coefficient can be calculated as

$$\sqrt{\frac{(T_{21} + \omega^2 Z_1 Z_2 T_{12})^2 + \omega^2 (Z_2 - Z_1)^2 T_{11}^2}{(T_{21} - \omega^2 Z_1 Z_2 T_{12})^2 + \omega^2 (Z_2 + Z_1)^2 T_{11}^2}}. \quad (23)$$

To achieve zero reflection, $T_{21} + \omega^2 Z_1 Z_2 T_{12}$ and T_{11} should be zero since $Z_2 \neq Z_1$. With Eq. (9), the transfer-matrix coefficient can be substituted into the zero reflection

condition. First, the $T_{11} = 0$ condition can be simplified as

$$T_{11} = \frac{\alpha_{\text{eff}}^i - \omega^2 m_{\text{eff}}^i}{\alpha_{\text{eff}}^i} = 0, \quad \alpha_{\text{eff}}^i = \omega^2 m_{\text{eff}}^i. \quad (24)$$

Also, $T_{21} + \omega^2 Z_1 Z_2 T_{12}$ condition can be simplified with Eqs. (9) and (24) as

$$\begin{aligned} T_{21} + \omega^2 Z_1 Z_2 T_{12} &= -\omega^2 m_{\text{eff}}^i + \omega^2 Z_1 Z_2 \frac{2\alpha_{\text{eff}}^i - \omega^2 m_{\text{eff}}^i}{\alpha_{\text{eff}}^i} \\ &= -\alpha_{\text{eff}}^i + \omega^2 Z_1 Z_2 \frac{1}{\alpha_{\text{eff}}^i} = 0. \end{aligned} \quad (25)$$

Therefore, the full-transmission condition can be described as the condition of effective mass, stiffness as

$$\alpha_{\text{eff}}^i = \pm \omega \sqrt{Z_1 Z_2}, \quad m_{\text{eff}}^i = \pm \sqrt{Z_1 Z_2} / \omega. \quad (26)$$

Here, substituting the full-transmission condition into the transmission coefficient, Eq. (20), the full transmission can be calculated as

$$\begin{aligned} \frac{2i\omega Z_1}{i\omega Z_2 T_{11} + T_{21} + i^2 \omega^2 Z_1 Z_2 T_{12} + i\omega Z_1 T_{22}} &= \frac{i\omega Z_1}{T_{21}} \\ &= \mp i \sqrt{\frac{Z_1}{Z_2}}. \end{aligned} \quad (27)$$

Similar to the first method, in this case, the transmission is also pure imaginary, which infers that only a constant phase shift of 90° and 270° can be achieved with full transmission. In other words, phase gradient based on the various phase shifts cannot be achieved with full transmission simultaneously by the previous methods.

III. A DOUBLE-UNIT METASURFACE FOR FULL-WAVE TAILORING IN THE INHOMOGENEOUS CASE

A. Design process of the double-unit metasurface components

To solve this issue, we propose a double-unit metasurface composed of two different units as in Fig. 1(c). Because two different units are required, the resulting double-unit metasurface can be thicker than desired. Thus, we utilize the previously developed single-unit metasurface, which has a single unit along the incident wave-propagating direction [14,26]. The unit, shown in Fig. 1(c), consists of vertical and horizontal resonators, which modulate the effective stiffness and mass, respectively [14,26]. As a result, the unit can be easily expressed by the simple mass-spring system shown in Figs. 2(b) and 2(c), whose effective spring coefficient α_{eff} and effective mass m_{eff} can be tailored by the heights of each resonator, h_{ver}

and h_{hor} , respectively. The detailed description of how each resonator affects the corresponding effective parameters are provided in Sec. III B. Based on the unit, the phase modulator and the impedance matcher are designed.

First, we design the phase modulator shown in Fig. 2(c). Because the phase modulator is located inside medium 1, the previous method for the homogeneous system [14,26] can be applied to achieve full transmission and various phase shifts simultaneously. For the current single mass-spring unit, it is shown that the effective mass and the corresponding phase shift under full transmission are [14,26]

$$m_{\text{eff}}^p = \frac{2\alpha_{\text{eff}}^p Z_1^2}{\alpha_{\text{eff}}^p{}^2 + \omega^2 Z_1^2},$$

$$\phi = \text{Arg} \left(\frac{\alpha_{\text{eff}}^p{}^2 - \omega^2 Z_1^2}{\alpha_{\text{eff}}^p{}^2 + \omega^2 Z_1^2} - \frac{2\alpha_{\text{eff}}^p \omega Z_1}{\alpha_{\text{eff}}^p{}^2 + \omega^2 Z_1^2} i \right). \quad (28)$$

Based on Eq. (28), the effective stiffness α_{eff}^p is defined for the desired phase shift values, and the corresponding effective mass m_{eff}^p is calculated. Subsequently, the phase-modulator unit is designed by adjusting h_{ver} and h_{hor} to achieve the desired effective parameters α_{eff}^p and m_{eff}^p . As a result, the phase modulator providing full transmission and the desired phase shifts can be designed.

Second, the impedance matcher in Fig. 2(b) is designed. Unlike the phase modulator, the impedance matcher is placed between two different media and designed to provide the full transmission only. As previously demonstrated, the effective parameters should follow Eq. (26) to achieve full transmission between different media. Because only one unit is required as an impedance matcher, we exploit the negative parameter case. In other words, the effective parameters for the full transmission are $\alpha_{\text{eff}}^i = -\omega\sqrt{Z_1 Z_2}$, $m_{\text{eff}}^i = -\sqrt{Z_1 Z_2}/\omega$. Note that in this full-transmission condition, the transmission becomes $i\sqrt{Z_1/Z_2}$, which infers that the phase shift is fixed as 90° so that the impedance matching layer does not affect the phase gradient. As in the phase-modulator design, an impedance matcher can be easily designed by adjusting h_{ver} and h_{hor} to achieve the desired α_{eff}^i and m_{eff}^i .

B. Resonator system for achieving the effective parameters

In the previous section, the required effective mass and spring coefficients to achieve full-wave tailoring between two different media are proposed. To realize these parameters with the actual continuum metasurface unit, we adopt a single metasurface unit with vertical and horizontal resonator systems [14,26]. In the metasurface unit, the effective mass and spring coefficients can be tuned from any negative to positive values by properly adjusting the horizontal and vertical resonator's configurations, respectively.

Here, let us review how the metasurface unit can achieve the desired effective mass and spring coefficients.

Figure 3 shows the actual resonator structure used in this work and the schematic mass-spring system to analysis the system theoretically. First, let us examine the diagonal spring, which couples the vertical and horizontal motions as can be seen in Fig. 3 [14,26,31]. The vertical and horizontal force and displacements are described as

$$\begin{pmatrix} F_x \\ F_y \end{pmatrix} = \begin{pmatrix} a & c \\ c & b \end{pmatrix} \begin{pmatrix} u_x \\ u_y \end{pmatrix} \quad \text{or} \quad \begin{pmatrix} F_x \\ F_y \end{pmatrix} = \begin{pmatrix} a & -c \\ -c & b \end{pmatrix} \begin{pmatrix} u_x \\ u_y \end{pmatrix}, \quad (29)$$

where F_x, F_y and u_x, u_y refer to the x, y -directional forces and displacements applied on the diagonal spring, respectively.

Again, assuming simple harmonic motion with an angular frequency ω , the dynamic equation of each mass can be derived as

$$-\omega^2 m_1 u_1 = \alpha_1 (u_o + u_d - 2u_1), \quad (30a)$$

$$-\omega^2 m_2 u_2 = a(u_o + u_d - 2u_2), \quad (30b)$$

$$-\omega^2 m_2 u_3 = a(u_o + u_d - 2u_3), \quad (30c)$$

$$-\omega^2 m_2 v_2 = -2bv_2 + c(u_o - u_d), \quad (30d)$$

$$-\omega^2 m_2 v_3 = -2bv_3 + c(u_d - u_o). \quad (30e)$$

By rearranging Eqs. (30a)–(30e), the displacements of each mass can be simplified as

$$u_1 = \frac{\alpha_1}{2\alpha_1 - \omega^2 m_1} (u_o + u_d), \quad (31a)$$

$$u_2 = u_3 = \frac{a}{2a - \omega^2 m_2} (u_o + u_d), \quad (31b)$$

$$v_2 = -v_3 = \frac{c}{2b - \omega^2 m_2} (u_o - u_d). \quad (31c)$$

As can be seen in Eqs. (31b) and (31c), the system behaves symmetrically along the y direction, which infers that only longitudinal directional displacement and force is generated at the unit. Also, in this work, the horizontal stiffness a is set to be high enough that $2a \gg \omega^2 m_2$ [14,26,31], which infers that the horizontal displacements of vertical resonators in Eq. (31b) can be simplified as $u_2 = u_3 =$

$(1/2)(u_o + u_d)$. Here, the boundary forces at the left and right boundaries can be calculated as

$$f_o = \alpha_1(u_1 - u_o) + a(u_2 + u_3 - 2u_o) + c(v_2 - v_3), \quad (32a)$$

$$f_d = \alpha_1(u_d - u_1) + a(2u_d - u_2 - u_3) + c(v_2 - v_3). \quad (32b)$$

By inserting Eqs. (31a)–(31c) into Eqs. (32a) and (32b), one can express the boundary forces as a function of the boundary displacements as

$$f_o = \alpha_1 \left[\left(\frac{\alpha_1}{2\alpha_1 - \omega^2 m_1} - 1 \right) u_o + \frac{\alpha_1}{2\alpha_1 - \omega^2 m_1} u_d \right] + \left(a - \frac{2c^2}{2b - \omega^2 m_2} \right) (u_d - u_o), \quad (33a)$$

$$f_d = \alpha_1 \left[\left(1 - \frac{\alpha_1}{2\alpha_1 - \omega^2 m_1} \right) u_d - \frac{\alpha_1}{2\alpha_1 - \omega^2 m_1} u_o \right] + \left(a - \frac{2c^2}{2b - \omega^2 m_2} \right) (u_d - u_o). \quad (33b)$$

According to Eqs. (8) and (9), the transfer matrix is defined as the relationship between the left and right boundary conditions. Therefore, Eqs. (33a) and (33b) should be rearranged in terms of u_d, f_d to achieve the transfer matrix as

$$u_d = \frac{\alpha_1 \left(1 - \frac{\alpha_1}{2\alpha_1 - \omega^2 m_1} \right) + a - \frac{2c^2}{2b - \omega^2 m_2}}{\frac{\alpha_1^2}{2\alpha_1 - \omega^2 m_1} + a - \frac{2c^2}{2b - \omega^2 m_2}} u_o + \frac{1}{\frac{\alpha_1^2}{2\alpha_1 - \omega^2 m_1} + a - \frac{2c^2}{2b - \omega^2 m_2}} f_o, \quad (34a)$$

$$f_d = \frac{\left(\alpha_1 + 2a - \frac{4c^2}{2b - \omega^2 m_2} \right) \left(\frac{-\omega^2 m_1}{2\alpha_1 - \omega^2 m_1} \right) \alpha_1}{\frac{\alpha_1^2}{2\alpha_1 - \omega^2 m_1} + a - \frac{2c^2}{2b - \omega^2 m_2}} u_o + \frac{\alpha_1 \left(1 - \frac{\alpha_1}{2\alpha_1 - \omega^2 m_1} \right) + a - \frac{2c^2}{2b - \omega^2 m_2}}{\frac{\alpha_1^2}{2\alpha_1 - \omega^2 m_1} + a - \frac{2c^2}{2b - \omega^2 m_2}} f_o. \quad (34b)$$

Therefore, the transfer matrix can be derived as

$$\mathbf{T} = \begin{pmatrix} \frac{\alpha_1 \left(1 - \frac{\alpha_1}{2\alpha_1 - \omega^2 m_1} \right) + a - \frac{2c^2}{2b - \omega^2 m_2}}{\frac{\alpha_1^2}{2\alpha_1 - \omega^2 m_1} + a - \frac{2c^2}{2b - \omega^2 m_2}} & \frac{1}{\frac{\alpha_1^2}{2\alpha_1 - \omega^2 m_1} + a - \frac{2c^2}{2b - \omega^2 m_2}} \\ \frac{\left(\alpha_1 + 2a - \frac{4c^2}{2b - \omega^2 m_2} \right) \left(\frac{-\omega^2 m_1}{2\alpha_1 - \omega^2 m_1} \right) \alpha_1}{\frac{\alpha_1^2}{2\alpha_1 - \omega^2 m_1} + a - \frac{2c^2}{2b - \omega^2 m_2}} & \frac{\alpha_1 \left(1 - \frac{\alpha_1}{2\alpha_1 - \omega^2 m_1} \right) + a - \frac{2c^2}{2b - \omega^2 m_2}}{\frac{\alpha_1^2}{2\alpha_1 - \omega^2 m_1} + a - \frac{2c^2}{2b - \omega^2 m_2}} \end{pmatrix}. \quad (35)$$

Here, recalling the transfer matrix in Eq. (9), one can notice that the effective parameters can be defined as

$$\frac{T_{21}}{-\omega^2} = m_{\text{eff}}, \quad \frac{T_{21}}{T_{11} - 1} = \alpha_{\text{eff}}. \quad (36)$$

Therefore, according to Eq. (36), the effective mass and stiffness can be calculated as

$$\alpha_{\text{eff}} = \alpha_1 + 2a - \frac{4c^2}{2b - \omega^2 m_2}, \quad (37a)$$

$$m_{\text{eff}} = \frac{\left(\alpha_1 + 2a - \frac{4c^2}{2b - \omega^2 m_2} \right) \left(\frac{m_1}{2\alpha_1 - \omega^2 m_1} \right) \alpha_1}{\frac{\alpha_1^2}{2\alpha_1 - \omega^2 m_1} + a - \frac{2c^2}{2b - \omega^2 m_2}}. \quad (37b)$$

As can be seen in Eq. (37a), the effective stiffness can be tuned from negative to positive value by the vertical resonance of the vertical resonator. On the other hand, the

effective mass is affected by both horizontal resonance of the horizontal resonator and vertical resonance of the vertical resonator. By adjusting each resonance mode, one can obtain the desired effective parameters for impedance matcher or phase modulators.

C. The actual metasurface design method

In the actual continuum metasurface unit, each parameters, such as α_1 , a , b , c , m_1 , and m_2 , are hard to be clearly defined. Thus, to clearly design the desired metasurface unit, we adopt a simple efficient size optimization algorithm called particle swarm optimization (PSO) to tailor the submass of each resonator, m_1 and m_2 , and corresponding submass heights, h_{hor} and h_{ver} , that provides desired effective mass and spring coefficients. The PSO algorithm was first introduced by Kennedy and Eberhart in 1995 [32]. The PSO algorithm, inspired from the social

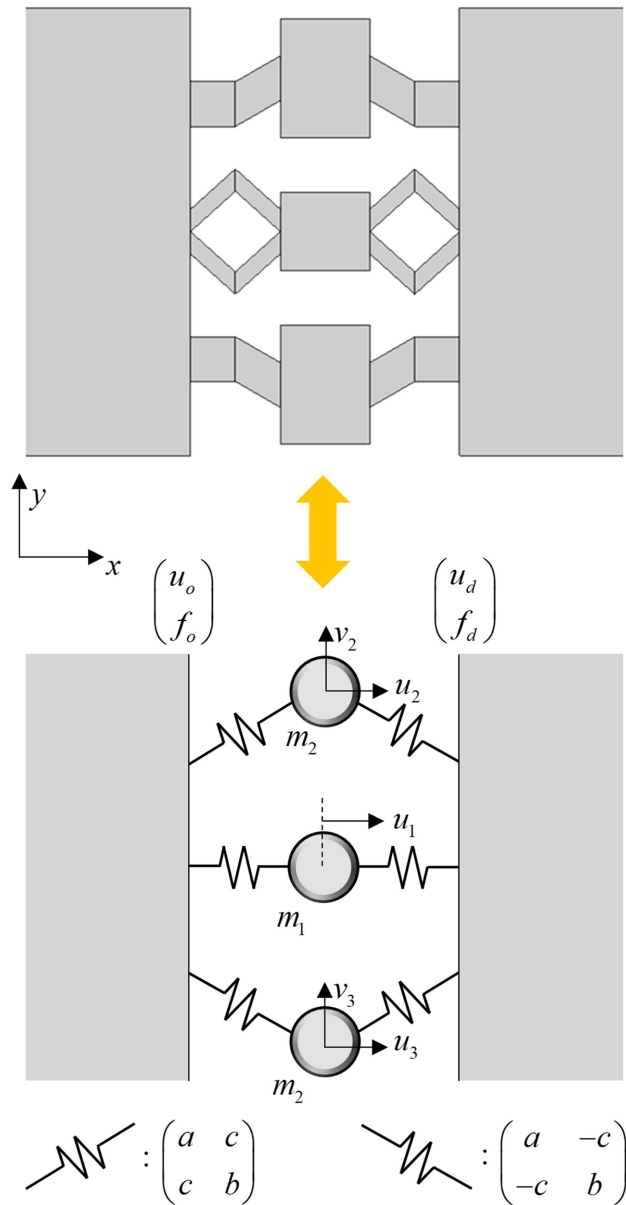


FIG. 3. Resonator structure and the schematic of the system.

behavior model of bioswarm such as bees or birds, is one of the representative optimization algorithms for complex optimization problems. In the PSO algorithm, each particle moves in multiple dimensional space to find the optimal function, using their information or interaction with nearby particles.

The optimization process in the PSO algorithm is basically carried out by movements of the particles. The individual particles update their locations and velocities at every loop of the algorithm. The velocities and locations are updated by information from the interaction between the particles. For n particles in the m -dimensional space, the locations of the particles are described as $\mathbf{X}_i^l =$

$[x_{i1}^l, \dots, x_{im}^l]$ and the velocities are described as $\mathbf{V}_i^l = [v_{i1}^l, \dots, v_{im}^l]$. The superscript l refers to the loop number in the algorithm process. The velocity and the location are updated as

$$\mathbf{V}_i^{l+1} = W\mathbf{V}_i^l + c_1\varepsilon_1(\mathbf{P}_i - \mathbf{X}_i^l) + c_2\varepsilon_2(\mathbf{G}_i - \mathbf{X}_i^l), \quad (38)$$

$$\mathbf{X}_i^{l+1} = \mathbf{X}_i^l + \mathbf{V}_i^l. \quad (39)$$

Here, the parameters c_1 and c_2 , controlling the velocity of the particles are empirically defined as 2.05. ε_1 and ε_2 take random values from 0 to 1. The variable W named as the inertial weight (usually 0 to 1 [33]), is updated as

$$W = W_{\max} - (W_{\max} - W_{\min})l/l_{\max}, \quad (40)$$

where W_{\max} and W_{\min} are defined as 1.1 and 0.1, respectively. As Eq. (38) shows, W controls the influence of the previous velocity on the current velocity; the larger W improves the global navigation while the smaller W improves the local navigation. As shown in Eq. (40), W is linearly decreased from the largest value at the earlier stage to the smallest value at the last stage.

In Eq. (38), the velocity is updated toward certain positions $\mathbf{P}_i = [P_{i1}, \dots, P_{im}]$ and $\mathbf{G} = [G_1, \dots, G_m]$. These two positions, \mathbf{P}_i and \mathbf{G} , which are called personal best and global best, respectively, are the most characteristic part of the PSO. The personal best is the position where the highest fitness is shown for the individual particle, while the global best is the position where the highest fitness is shown of the entire swarm. In other words, the global best can be updated as the best value among the values of the personal bests at every loop. At every iteration, the particles derive the global best by communicating each other, updating their velocities using the global best and the personal best. Finally, the global best is returned at the optimal position when the loop number l reaches l_{\max} .

For the phase modulator, the objective function is chosen to optimize both the transmission and phase shifts as

$$f(\mathbf{X}) = |T(\mathbf{X}) - 1| + |\phi(\mathbf{X}) - \phi_k|. \quad (41)$$

Also, for the impedance matcher, the objective function is set to minimize the reflection as

$$f(\mathbf{X}) = R(\mathbf{X}) = \sqrt{1 - T^2(\mathbf{X}) \times Z_2/Z_1}. \quad (42)$$

It is worthwhile to note that PSO optimization has a random process so that its result can be varied if the optimization setting changes. Furthermore, the PSO optimization may provide unsatisfactory results. Thus, in the PSO optimization process, we establish the design criteria for the transmission as $T(\mathbf{X}) > 0.9$ and for the phase difference $|\phi(\mathbf{X}) - \phi_k| < 0.1$. Based on this criterion, we execute PSO optimization multiple times until the optimized design satisfies the design criteria.

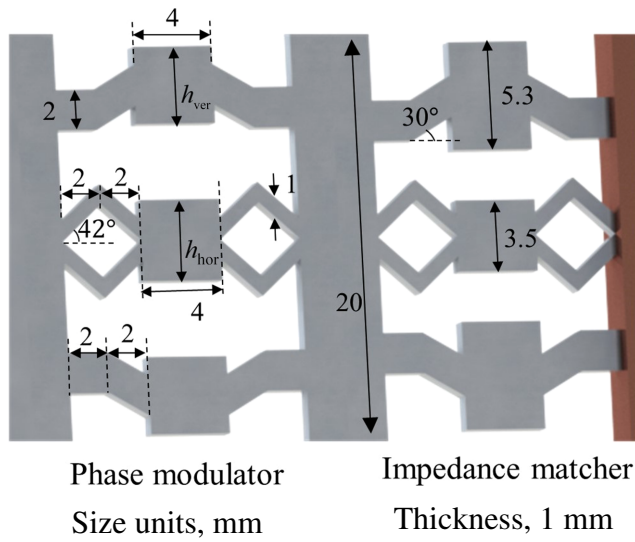


FIG. 4. The specific geometric condition of the real structure.

As an example, we design the double-unit metasurface for wave-front tailoring between 1- and 3-mm-thick aluminum plates for the 50-kHz longitudinal wave. Note that for the longitudinal wave, the mechanical impedance is defined as $Z = \rho cA$. Thus, although both plates have the same material, two plates having different thicknesses have different impedances [34].

Setting the target phase gradient as 12.5π rad/m, the eight phase modulators with the phase shift of $\phi = 0, 0.25\pi, 0.5\pi, 0.75\pi, \pi, 1.25\pi, 1.5\pi,$ and 1.75π rad are considered. The geometry of each unit earned by the PSO algorithm is described in Fig. 4 and Table I. The target and realized values of phase shifts and transmission ratio are compared in Table I. As shown, every phase-modulator unit has the transmission ratio over 0.9. Also, the impedance matcher shows the transmission ratio of 0.572, which infers full transmission is achieved compared to the theoretical full-transmission ratio, 0.577.

TABLE I. The specific geometry of each unit and comparison between the ideal and realized transmission ratio, phase shift. The white cells show each phase modulators' specifications and the shadowed cell shows the specification of the impedance matcher.

Ideal ϕ	Realized ϕ	Realized $ T $	h_{ver} (mm)	h_{hor} (mm)
0	0.059π	0.993	4.0	4.4
0.25π	0.238π	0.935	3.8	4.0
0.5π	0.458π	0.998	3.7	3.6
0.75π	0.764π	0.975	3.2	3.5
π	1.025π	0.992	2.1	3.4
1.25π	1.211π	0.902	5.8	3.4
1.5π	1.600π	0.947	4.8	3.0
1.75π	1.841π	0.999	4.2	2.2
0.5π	0.677π	0.572	5.3	3.5

IV. NUMERICAL VALIDATIONS OF THE MASS-SPRING UNIT CELLS AND THE METASURFACE

To check whether the phase modulators and impedance matcher are well designed, the one-dimensional wave simulations for each case are carried out. In simulations, a 50-kHz longitudinal wave is considered as the incident wave. (Strictly, the whole system is three dimensional so the wave is the lowest-order symmetric Lamb-wave mode, S0-wave mode [34]. However, at 50 kHz, the S0 waves in 1- and 3-mm-thick aluminum plates are almost nondispersive and can be described by the longitudinal wave under the plane stress [34,35]. In our paper, the term “longitudinal wave” is used instead of the S0-wave mode for the simplification.)

Figure 5(a) shows the detailed numerical simulation settings for the phase modulators or impedance matcher. To perfectly simulate the one-dimensional plane-wave case, the continuity condition is imposed at both upper and lower

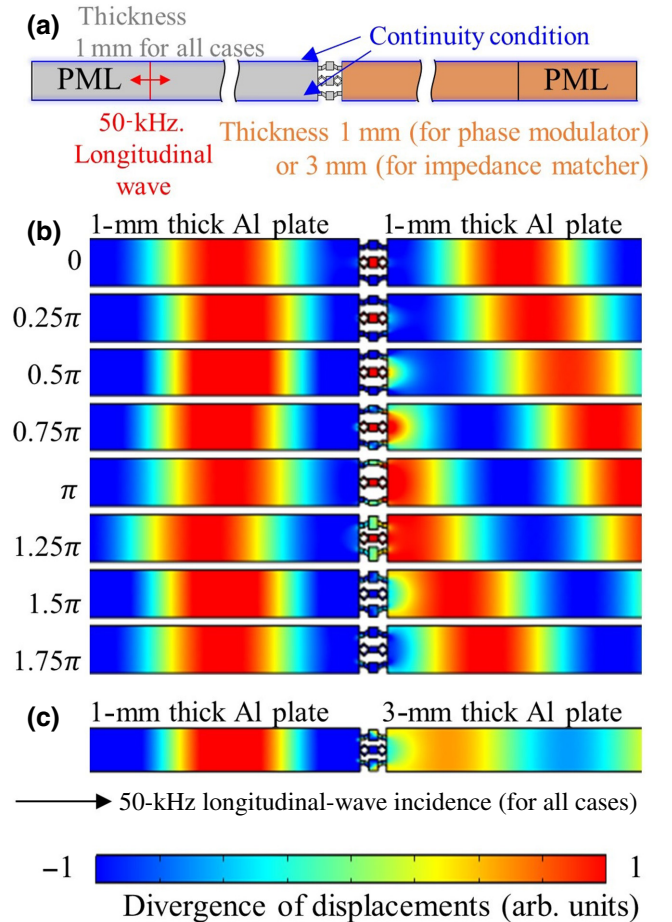


FIG. 5. (a) Simulation setting for the phase modulator or impedance matcher and numerical result showing the transmission and phase shift for (b) phase modulators in a single medium, (c) impedance matcher connecting different media.

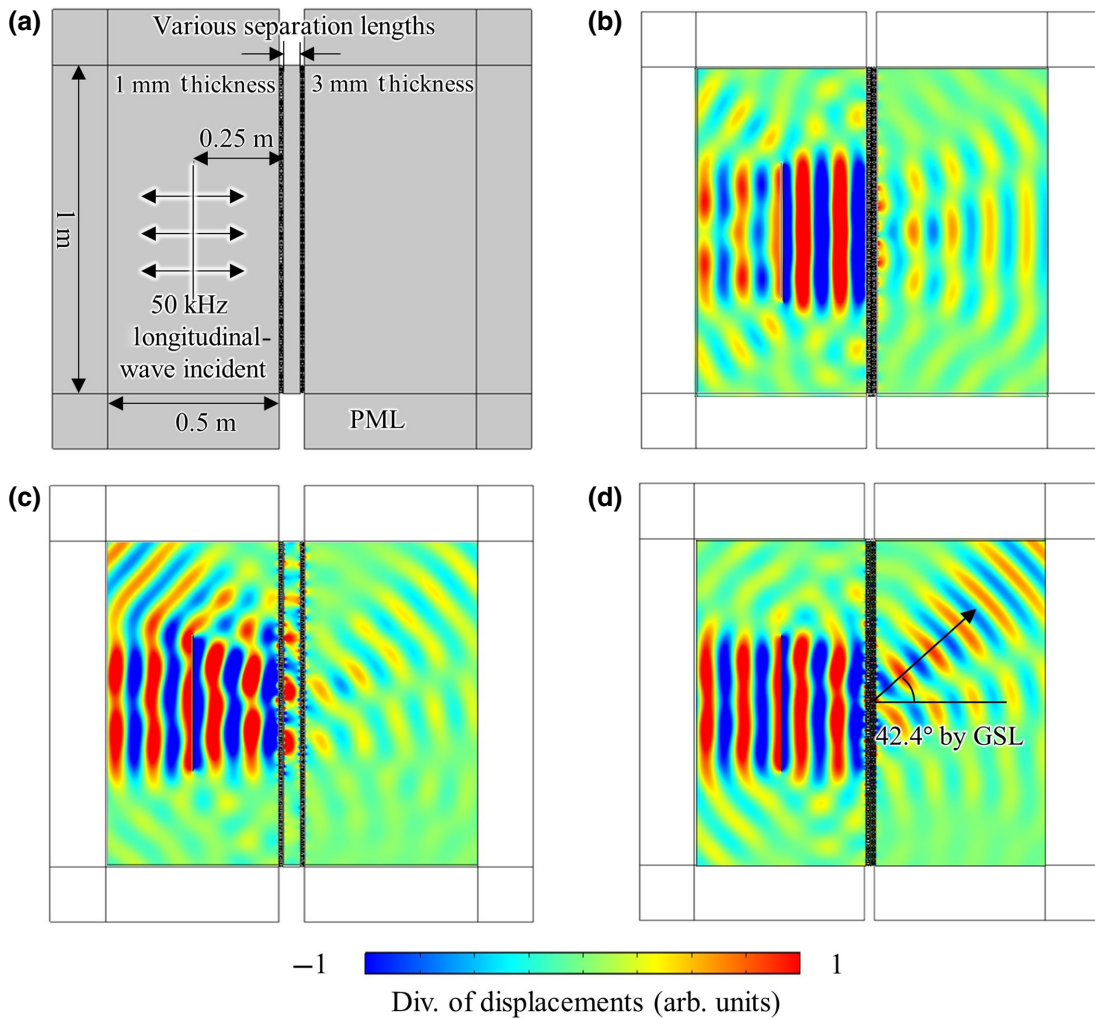


FIG. 6. (a) Numerical simulation setting, and the results with 50-kHz longitudinal waves with various separation of (b) 0.001 m, (c) 0.05 m, and (d) 0.004 m, respectively.

boundaries so that the unit is considered to be infinitely arranged along the vertical direction. Also, the perfectly matched layer (PML) is placed at the left and right end to prevent any undesired reflections. At the interface between incident field and the left PML, the 50-kHz longitudinal wave is excited. In the simulation, the time-harmonic simulation is carried out with the commercial software, COMSOL Multiphysics. After the simulation, the well-known two-point method [36] is used to calculate the amount of transmission and phase shift achieved by the unit cell.

The simulation results for the phase modulators tuned to render variable phase shifts from 0 to 1.75π rad are depicted in Fig. 5(b). Here, the amplitudes at the right side of the phase modulators are almost the same with the amplitude at the left side, which implies that almost full transmission is indeed achieved for all phase-modulator designs. Figure 5(c) shows the simulation result for the impedance matcher. Interestingly, the amplitude at the right side has decreased compared to the amplitude on

the left side. This is because the wave media are different; the left side of the unit is a 1-mm-thick aluminum plate, whereas the right side is a 3-mm-thick aluminum plate. Thus, although the full transmission is achieved, the amplitude at the right side is decreased. As aforementioned, the amplitude ratio of the transmitted and incident waves is 0.572, which is almost the same as the theoretical value under the full transmission, 0.577, suggesting that almost full transmission is achieved between two different media by implementing the impedance matching layer.

Following the successful design of the phase modulator and the impedance matcher, a double-unit metasurface is designed by combining two units. In the combination, the separation between two units is a useful factor. If the separation is too narrow, the resonators in each unit may get coupled to each other and the double-unit device will not work. Conversely, if the separation is too wide, the transmitted waves from the phase modulator will be fully developed, and form refracted longitudinal and shear

waves. Because the impedance matcher is designed for the normally incident longitudinal wave, these fully developed waves will deteriorate the performance of the impedance matcher.

To find the proper size of the separation, numerical simulations with various separation sizes are carried out. Figure 6 shows the wave-simulation setting and results with various separations. In Fig. 6(a), the numerical simulation settings are shown. At every edge, the PML is attached to prevent unwanted reflected waves. The metasurface, consisting of the phase modulators and impedance matcher, is placed between 1- and 3-mm aluminum plate whose sizes are $0.5 \text{ m} \times 1 \text{ m}$, large enough to see the wave propagation inside. At the center of the whole field, the metasurface with various separation size is installed. At the 1-mm aluminum plate, the wave source having 0.5 m width is located 0.25 m from the metasurface, and actuated with 50-kHz longitudinal wave. Again, the time-harmonic simulation is carried out with COMSOL Multiphysics.

As stated earlier, if the separation is too narrow [as in Fig. 6(b) where the separation is 1 mm] or too broad [as in Fig. 6(c) where the separation is 50 mm], the designed double-unit metasurface does not work well. We simulate with various separation distances and settle on a double-unit metasurface with a separation of 4 mm for satisfactory performance. Figure 6(d) plots the wave-simulation result of the designed double-unit metasurface between 1- and 3-mm-thick aluminum plate. Wave-front tailoring is clearly achieved between two different media with almost full transmission, which is impossible with the previous methods. Of course, the refraction angle agrees well with the theoretically predicted angle by the generalized Snell's law (GSL), 42.4° .

V. EXPERIMENTS

Finally, the experimental realization of the proposed metasurface is conducted. A schematic diagram of the experimental setup is shown in Fig. 7(a). The proposed metasurface is fabricated at the edge of a 1-mm -thick aluminum plate by laser-beam machining (Bysprint Fiber 3015, Bystronic) and directly bonded to a 3-mm -thick aluminum plate with shear gel couplant (H-2, OLYMPUS). Both plates have the same horizontal and vertical size, $1 \text{ m} \times 1 \text{ m}$. As the longitudinal motion requires symmetry along the direction corresponding to the thickness of the plates, we ensure that the symmetry is maintained after bonding the two plates. As can be seen in Fig. 7(a), the measurement points (white circles) are located on the 3-mm plate for every 15° and 0.4 m away from the center of the fabricated metasurface. The electromagnetic acoustic transducer (EMAT) and piezoelectric transducer patch are adopted as the wave sensor and source to measure and generate the 50-kHz longitudinal wave, respectively. The EMAT sensor is direction-selective in-plane mode

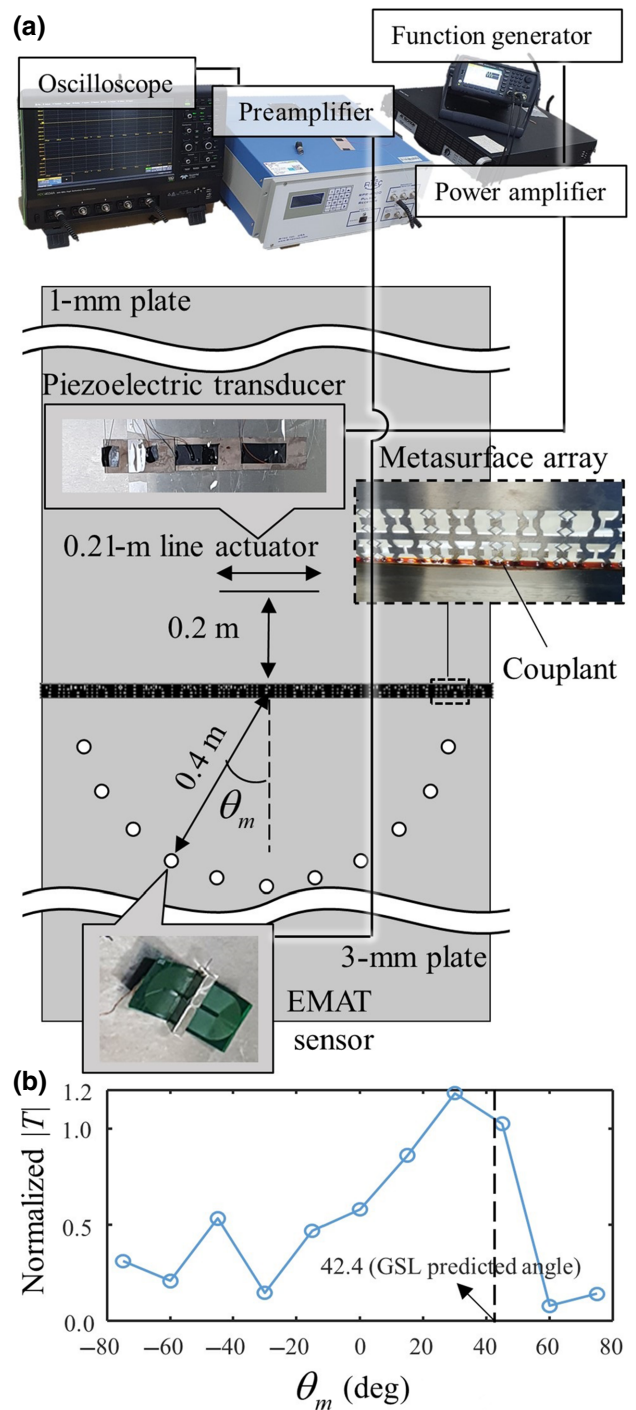


FIG. 7. (a) Schematic of experimental setups. (b) Normalized amplitudes of the experimentally measured longitudinal waves.

transducer, which can neglect the unwanted shear or flexural wave modes. Since the undesired flexural wave is not measured, piezoelectric transducers can be used as the longitudinal-wave source in the current experiments. By Poisson's effect, the piezoelectric transducers generate the longitudinal wave, although the piezoelectric transducers simultaneously generate flexural waves, which can be

filtered by the EMAT sensor. In other words, the piezoelectric transducer also generates flexural waves; however, they are automatically filtered out since EMAT cannot measure the flexural wave. The detailed experimental procedure is as follows. First, we generate and amplify a ten-cycle sinusoidal input signal by the function generator (33 250B, Keysight) and the signal is amplified by the power amplifier (7224 power amplifier, AE techron). Then the signal is sent to the piezoelectric actuator, which generates the desired longitudinal wave in a plate. After the actuation, the transmitted longitudinal waves are measured by the EMAT receiver. The measured data is amplified by the preamplifier (RPR-4000, Ritec), and recorded by the oscilloscope (WaveRunner 104MXi-A, Lecroy). Finally, the measured data are postprocessed by fast Fourier transformation to evaluate the amplitudes of the 50-kHz component only at every measurement point.

To check the degree of transmission, the measured transmitted wave is normalized by the amount of the incident wave. However, it requires special treatment as the amplitude of the incident wave is difficult to measure. To check the wave transmission experimentally, we perform additional experiment with the same experimental setting and the same bonding condition, but without the metasurface. This corresponds to the well-known case of longitudinal wave at two different media; hence, the transmission can be predicted theoretically. As a result, we can predict the amount of the ideal signal amplitude of the fully transmitted wave with a simple calculation. Figure 7(b) shows the experimentally and numerically measured normalized amplitude of the transmitted longitudinal wave. The experimentally measured signal near the predicted angle, 42.4° , is approximately 118% of the predicted transmission signal because the wave energy is focused as the beam width becomes more compact. This implies that almost full transmission is realized with the wave-front tailoring.

VI. CONCLUSION

In this paper, we propose a method to achieve wave-front tailoring between two different media. First, we show that the previous methods in elastic metasurfaces cannot be applied for the inhomogeneous cases. To overcome this limitation, we propose the double-unit metasurface consisting of phase modulator and impedance matcher. In this configuration, the phase modulator provides proper phase shifts to tailor wave front, whereas the impedance matcher provides full transmission between two different media. Based on the equivalent mass-spring system, the phase modulator and the impedance matcher are designed with proper separation. Numerical and experimental validations show that the designed double-unit metasurface can effectively tailor wave front with almost full transmission between two different media. Our proposed metasurface will potentially allow advances in various ultrasonic

applications such as nondestructive evaluation, vibration tailoring, ultrasonic imaging, and transducers.

ACKNOWLEDGMENTS

This work is supported by the Center for Advanced Meta-Materials (CAMM) funded by the Ministry of Science, ICT and Future Planning as Global Frontier Project (CAMM-2014M3A6B3063711), by the National Research Foundation of Korea (NRF) grants funded by the Korean government (Grants No. 2021R1A4A1033224, No. 2020R1A2C4002383, and No. 2020M3F6A108180512), by the National Research Council of Science & Technology (NST) grant by the Korean government (MSIP; No. CAP-17-04-KRISS). We would like to thank Editage [37] for editing and reviewing this paper for English language.

-
- [1] N. Yu, P. Genevet, M. Kats, F. Aieta, J. Tetienne, F. Capasso, and Z. Gaburro, Light propagation with phase discontinuities: Generalized laws of reflection and refraction, *Science* **334**, 333 (2011).
 - [2] T. Pertsch, T. Zentgraf, U. Peschel, A. Bräuer, and F. Lederer, Anomalous Refraction and Diffraction in Discrete Optical Systems, *Phys. Rev. Lett.* **88**, 093901 (2002).
 - [3] N. K. Grady, J. E. Heyes, D. R. Chowdhury, Y. Zeng, M. T. Reiten, A. K. Azad, A. J. Taylor, D. A. R. Dalvit, and H. T. Chen, Terahertz metamaterials for linear polarization conversion and anomalous refraction, *Science* **340**, 1304 (2013).
 - [4] F. Monticone, N. M. Estakhri, and A. Alù, Full Control of Nanoscale Optical Transmission With a Composite Metascreen, *Phys. Rev. Lett.* **110**, 203903 (2013).
 - [5] C. Pfeiffer and A. Grbic, Metamaterial Huygens' Surfaces: Tailoring Wave Fronts With Reflectionless Sheets, *Phys. Rev. Lett.* **110**, 197401 (2013).
 - [6] F. Aieta, M. A. Kats, P. Genevet, and F. Capasso, Multi-wavelength achromatic metasurfaces by dispersive phase compensation, *Science* **347**, 1342 (2015).
 - [7] S. Sun, K. Y. Yang, C. M. Wang, T. K. Juan, W. T. Chen, C. Y. Liao, Q. He, S. Xiao, W. T. Kung, G. Y. Guo, L. Zhou, and D. P. Tsai, High-efficiency broadband anomalous reflection by gradient meta-surfaces, *Nano Lett.* **12**, 6223 (2012).
 - [8] Z. Li, E. Palacios, S. Butun, and K. Aydin, Visible-frequency metasurfaces for broadband anomalous reflection and high-efficiency spectrum splitting, *Nano Lett.* **15**, 1615 (2015).
 - [9] F. Aieta, P. Genevet, N. F. Yu, M. A. Kats, Z. Gaburro, and F. Capasso, Out-of-plane reflection and refraction of light by anisotropic optical antenna metasurfaces with phase discontinuities, *Nano Lett.* **12**, 1702 (2012).
 - [10] J. Zhao, B. Li, Z. Chen, and C. W. Qiu, Manipulating acoustic wavefront by inhomogeneous impedance and steerable extraordinary reflection, *Sci. Rep.* **3**, 2537 (2013).

- [11] Y. Li, B. Liang, Z. M. Gu, X. Y. Zou, and J. C. Cheng, Reflected wavefront manipulation based on ultrathin planar acoustic metasurfaces, *Sci. Rep.* **3**, 2546 (2013).
- [12] L. Cao, Z. Yang, Y. Xu, and B. Assouar, Deflecting flexural wave with high transmission by using pillared elastic metasurface, *Smart Mater. Struct.* **27**, 075051 (2018).
- [13] H. Lee, J. K. Lee, H. M. Seung, and Y. Y. Kim, Mass-stiffness substructuring of an elastic metasurface for full transmission beam steering, *J. Mech. Phys. Solids.* **112**, 577 (2018).
- [14] S. W. Lee and J. H. Oh, Single-layer elastic metasurface with double negativity for anomalous refraction, *J. Phys. D: Appl. Phys.* **53**, 265301 (2020).
- [15] X. Ni, A. V. Kildishev, and V. M. Shalaev, Metasurface holograms for visible light, *Nat. Commun.* **4**, 2807 (2013).
- [16] Y. Tian, Q. Wei, Y. Cheng, and X. Liu, Acoustic holography based on composite metasurface with decoupled modulation of phase and amplitude, *Appl. Phys. Lett.* **110**, 191901 (2017).
- [17] S. W. Fan, Y. F. Zhu, L. Y. Cao, Y. F. Wang, A. L. Chen, A. Merkel, Y. S. Wang, and B. Assouar, Broadband tunable lossy metasurface with independent amplitude and phase modulations for acoustic holography, *Smart Mater. Struct.* **29**, 105038 (2020).
- [18] Y. Yang, H. Wang, F. Yu, Z. Xu, and H. Chen, A metasurface carpet cloak for electromagnetic, acoustic and water waves, *Sci. Rep.* **6**, 20219 (2016).
- [19] P. Y. Chen, J. Soric, Y. R. Padooru, H. M. Bernety, A. B. Yakovlev, and A. Alù, Nanostructured graphene metasurface for tunable terahertz cloaking, *New J. Phys.* **15**, 123029 (2013).
- [20] S. Zhai, H. Cheng, C. Ding, L. Li, F. Shen, C. Luo, and X. Zhao, Ultrathin skin cloaks with metasurfaces for audible sound, *J. Phys. D: Appl. Phys.* **49**, 225302 (2016).
- [21] S. W. Fan, S. D. Zhao, L. Cao, Y. Zhu, A. L. Chen, Y. F. Wang, K. Donda, Y. S. Wang, and B. Assouar, Reconfigurable curved metasurface for acoustic cloaking and illusion, *Phys. Rev. B* **101**, 024104 (2020).
- [22] M. S. Kim, W. R. Lee, Y. Y. Kim, and J. H. Oh, Transmodal elastic metasurface for broad angle total mode conversion, *Appl. Phys. Lett.* **112**, 241905 (2018).
- [23] H. Zhu and F. Semperlotti, Anomalous Refraction of Acoustic Guided Waves in Solids with Geometrically Tapered Metasurfaces, *Phys. Rev. Lett.* **117**, 034302 (2016).
- [24] Y. Liu, Z. Liang, F. Liu, O. Diba, A. Lamb, and J. Li, Source Illusion Devices for Flexural Lamb Waves Using Elastic Metasurfaces, *Phys. Rev. Lett.* **119**, 034301 (2017).
- [25] M. Zheng, C. I. Park, X. Liu, R. Zhu, G. Hu, and Y. Y. Kim, Non-resonant metasurface for broadband elastic wave mode splitting, *Appl. Phys. Lett.* **116**, 171903 (2020).
- [26] S. W. Lee, H. M. Seung, W. Choi, M. Kim, and J. H. Oh, Broad-angle refractive transmodal elastic metasurface, *Appl. Phys. Lett.* **117**, 213502 (2020).
- [27] E. Bok, J. J. Park, H. Choi, C. K. Han, O. B. Wright, and S. H. Lee, Metasurface for Water-to-Air Sound Transmission, *Phys. Rev. Lett.* **120**, 044302 (2018).
- [28] A. H. Dorrah, M. Chen, and G. V. Eleftheriades, Bianisotropic Huygens' metasurface for wideband impedance matching between two dielectric media, *IEEE Trans Antennas. Propag.* **66**, 4729 (2018).
- [29] T. G. Álvarez-Arenas, Acoustic impedance matching of piezoelectric transducers to the air, *IEEE Trans Ultrason. Ferroelectr. Freq. Control* **51**, 624 (2004).
- [30] T. E. Gómez and F. Montero, Bridging the gap of impedance mismatch between air and solid materials, *IEEE Ultrason. Symp.* **2**, 1069 (2000).
- [31] J. H. Oh, Y. E. Kwon, H. J. Lee, and Y. Y. Kim, Elastic metamaterials for independent realization of negativity in density and stiffness, *Sci. Rep.* **6**, 23630 (2016).
- [32] J. Kennedy and R. Eberhart, Particle swarm optimization, *Proc. IEEE Int. Conf. Neural Netw.* **4**, 1942 (1995).
- [33] C. Arora and S. S. Pattnaik, Particle swarm optimization based metamaterial inspired circularly polarized patch antenna for S band applications, *Evol. Intell.* **14**, 801 (2021).
- [34] K. F. Graff, *Wave Motion in Elastic Solids* (Dover, New York, 1975).
- [35] S. H. Díaz-Valdés and C. Soutis, Real-time nondestructive evaluation of fiber composite laminates using low-frequency lamb waves, *J. Acoust. Soc. Am.* **111**, 2026 (2002).
- [36] Y. Goda and Y. Suzuki, Estimation of incident and reflected waves in random wave experiments, *Coast. Eng.* **1976**, 828 (1977).
- [37] www.editage.co.kr.